Supporting Information

Preparation of electrodes and electrolyte. S-KB composite was obtained by homogenously mixing sulfur powder (99.99%, Sigma-Aldrich) and Ketjenblack carbon black (KB, AkzoNobel) and applying a simple heat treatment (155°C), which incorporate sulfur into the porous matrix by melt diffusion. The mass radio of S and KB was 5:4. Composite S-KB anodes were fabricated by compressing S-KB composite and poly(vinylidenedifluoride) (PTFE) at a weight ratio of 9:1 on an aluminum mesh (200 mesh). The areal loading of sulfur was ~8 mg cm^{-2}. Composite $LiMn_2O_4$ and HV-$LiCoO_2$ cathodes were fabricated by compressing active material powder (MTI Corporation), carbon black, and PTFE at weight ratio of 8:1:1 on a stainless steel grid. The aqueous electrolytes were prepared by dissolving 21 mol kg^{-1} LiTFSI (>98%, TCI Co., Ltd.) in water (HPLC grade), in which an additional 7 mol kg^{-1} LiOTf (>99.996%, Sigma-Aldrich) was dissolved to make the water-in-bisalt electrolyte. Aqueous gel electrolytes were prepared by adding 10 wt.% polyvinyl alcohol (PVA, Sigma-Aldrich) in the liquid water-in-bisalt electrolyte and heated at 95 ° C for 5 h under vigorous stirring. Prior to cell assembly, electrodes and the separator were soaked with the hot gel and then allowed to solidify at room temperature for 10 h.

Electrochemical measurements. The aqueous three-electrode devices for both anode and cathode materials consist of the test material as working electrode, active carbon (about 20 times mass of working) as the counter electrode, Ag/AgCl as the reference electrode, and WiBS solution (21 mol kg^{-1} LiTFSI + 7 mol kg^{-1} LiOTf) as electrolyte. The "m" is molality standing for mol-salt in Kg-solvent. The potential was converted into a scale against Li reference for convenience of comparison. The reference non-aqueous Li/S half cells were assembled in a CR2032-type coin cell using the same S-KB electrode as the cathode, lithium foil as the anode, and a typical electrolyte of 1M LiTFSI in 1,2-dimethoxyethane/1,3-dioxolane (DME/DOL, 1:1 vol%) and 2 wt% $LiNO_3$. Cyclic voltammetry was carried out using a CHI 600E electrochemical work station. The Li-ion/S full cell was assembled as a CR2032-type coin cell using either $LiMn_2O_4$ or $LiCoO_2$ as the cathode, S-KB as the anode, and glass fiber as the separator.

The cathode/anode mass ratios were set at 6.90:1 for S/$LiMn_2O_4$ cell and 4.51:1 for S/$LiCoO_2$ cell. The cells were cycled galvanostatically on a Land BT2000 battery test system (Wuhan, China) at room temperature. The GITT experiment was performed in a two-electrode full cell, with the capacity of the $LiMn_2O_4$ cathode being five times that of the anode to avoid the interference from its two plateaus. The cycling protocol consists in 0.1C current pulses for 10 min alternated with 60 min OCV periods.

Characterization. *In-situ* Raman spectra were collected with a Horiba Jobin Yvon Labram Aramis using a HeNe laser (632.8 nm) between 700 and 60 cm^{-1}. For this characterization, a $LiMn_2O_4$/S full cell was assembled in a well-sealed quartz tube and connected to a galvanostatic battery test system. X-ray photoelectron spectroscopic (XPS) analysis was performed with a high resolution Kratos AXIS 165 X-ray photoelectron spectrometer using monochromic AlKα radiation. Scanning electron microscopy (SEM) of the anode was performed in a Hitachi S-4700 operating at 5 kV. Transmission electron microscopy (TEM) were conducted on a JEOL (Japan) 2100F field emission. The tested S-KB anodes were retrieved from the full cells at different SOCs, then soaked in DME for 1 min to remove most of residual electrolyte. The anion spices were characterized with electrospray ionization time of flight mass spectrometry (AccuTOF, JEOL, USA, Inc.). Mass spectra were acquired under negative mode in *m/z* ranging from 12 to 250 with following parameters: capillary voltage, 2100V; orifice 1 voltage, 20V; orifice 2 voltage, 5V; ring voltage, 5V; dissolution temperature 100oC.

Molecular Dynamics Simulations. Molecular dynamics (MD) simulations were performed on 4m Li_2S_2 or Li_2S_4 dissolved in WiBS aqueous electrolyte (21 mol kg^{-1} LiTFSI +7 mol kg^{-1} LiOTf) at 333 K utilizing many-body polarizable force field as discussed in details as below.

Supplementary figures and tables for the experimental part:

Figures S1 – S16 and Tables S1 – S2

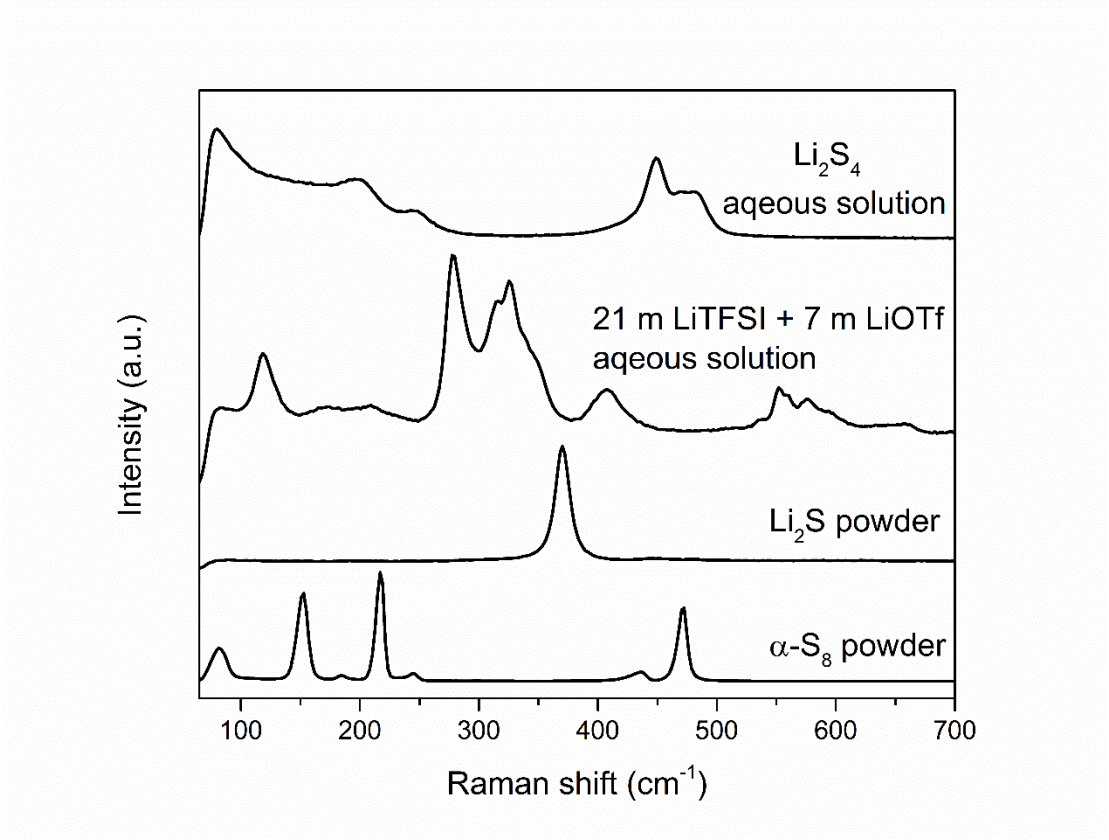

Figure S1. Raman spectra of elemental sulfur powder, Li_2S powder, electrolyte, and Li_2S_4 aqueous solution.

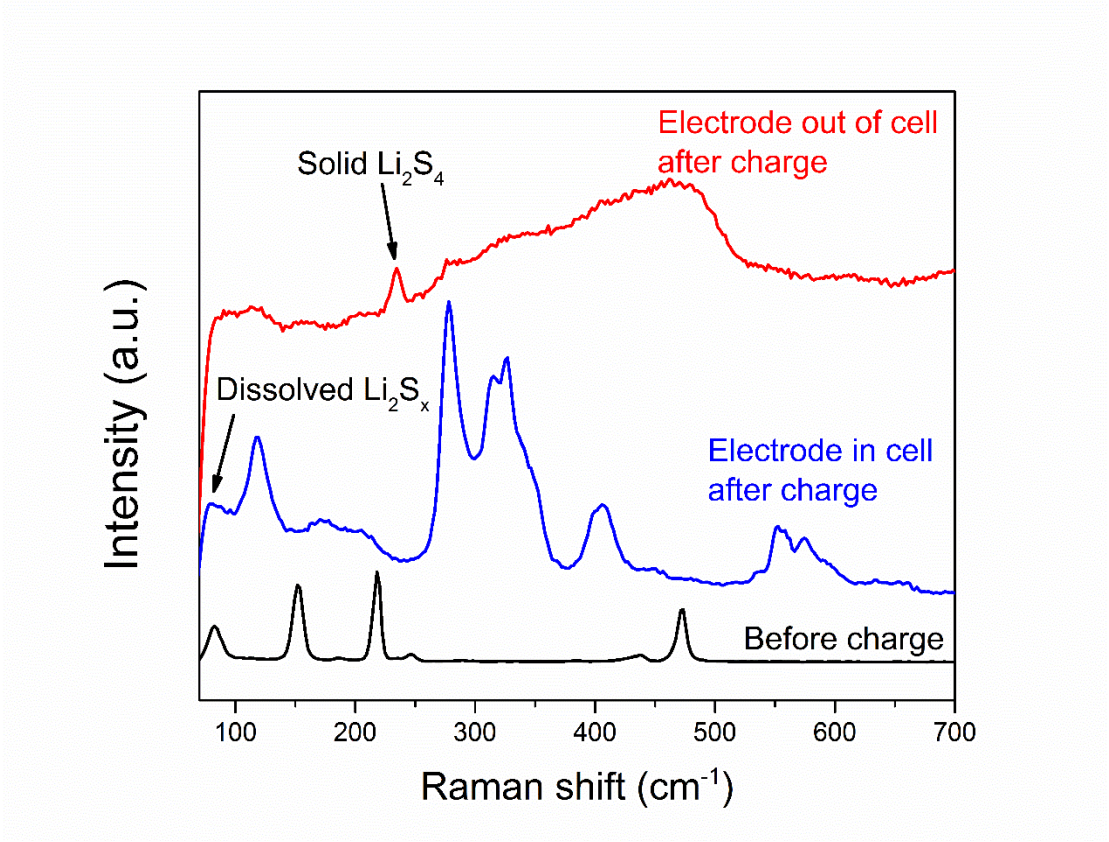

Figure S2. Raman spectra of sulfur anode with elemental sulfur dip-coated aluminum mesh as anode in full cell before and after being charged at the rate of 0.2 C. Before charge, the Raman spectra of S@Al electrode showed only the signal of elemental sulfur. After charge in the cell, the signal of elemental sulfur on S@Al electrode in the cell disappeared along with the appearance of dissolved polysulfide. However, after taking electrode the charged S@Al out of electrolyte and washing with DME, the Raman spectra of electrode showed trace of solid short-chain polysulfide.

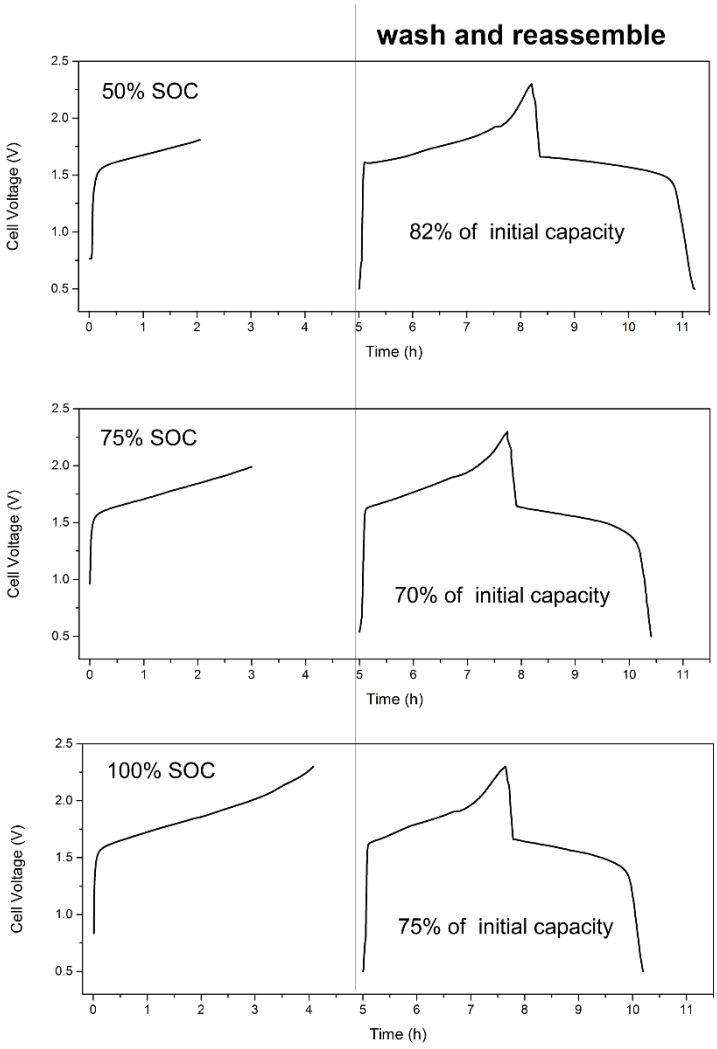

Figure S3. The voltage profiles of S-KB and $LiMn_2O_4$ full cell before and after reassembling. Firstly, the cells were charged to different state of charge (SOC) in WiBS electrolyte. Then the S-KB electrodes were taken out and washed by anhydrous DME for several times. DME was known as a low solubility solvent for short-chain LiPS. After washing, all liquid phase LiPS should be removed. The new cells with these electrodes were reassembled with fresh WiBS electrolyte, fully discharged and tested for new cycles at same current again. The new voltage profiles were similar with the initial ones, with > 70% of initial capacities remaining. This is a clear evident for solid-liquid mixed phase of LiPS, most of which is in solid phase.

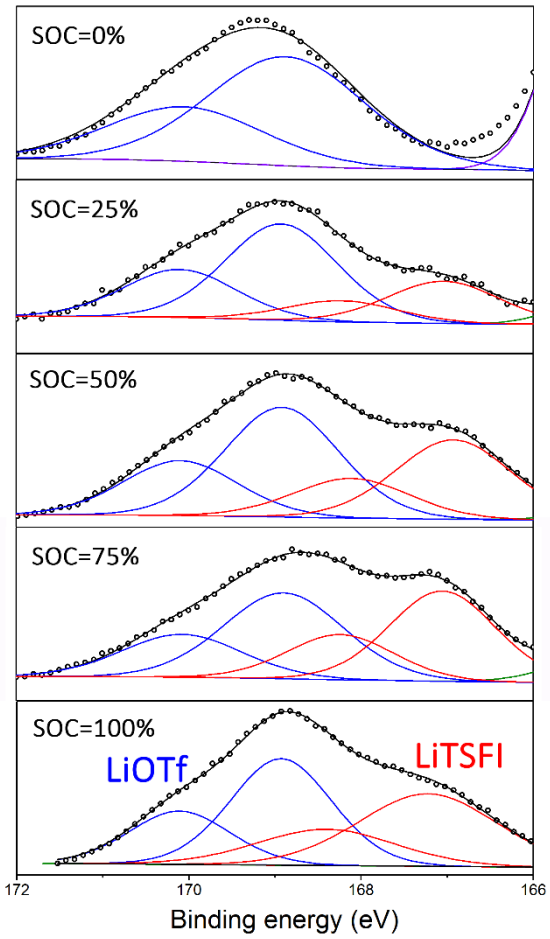

Figure S4. *Ex-situ* XPS S 2*p* spectra of S/KB anode with the binding energy over 166 eV in full cell after charge to specific states. Black dotted lines are experimental data, black lines are overall fitted data, and solid lines in other colors are fitted individual environments in salt anions: $2p_{3/2\text{-blue}}$(LiOTf) 168.9 eV and $2p_{3/2\text{-red}}$(LiTFSI) 167.2 eV.

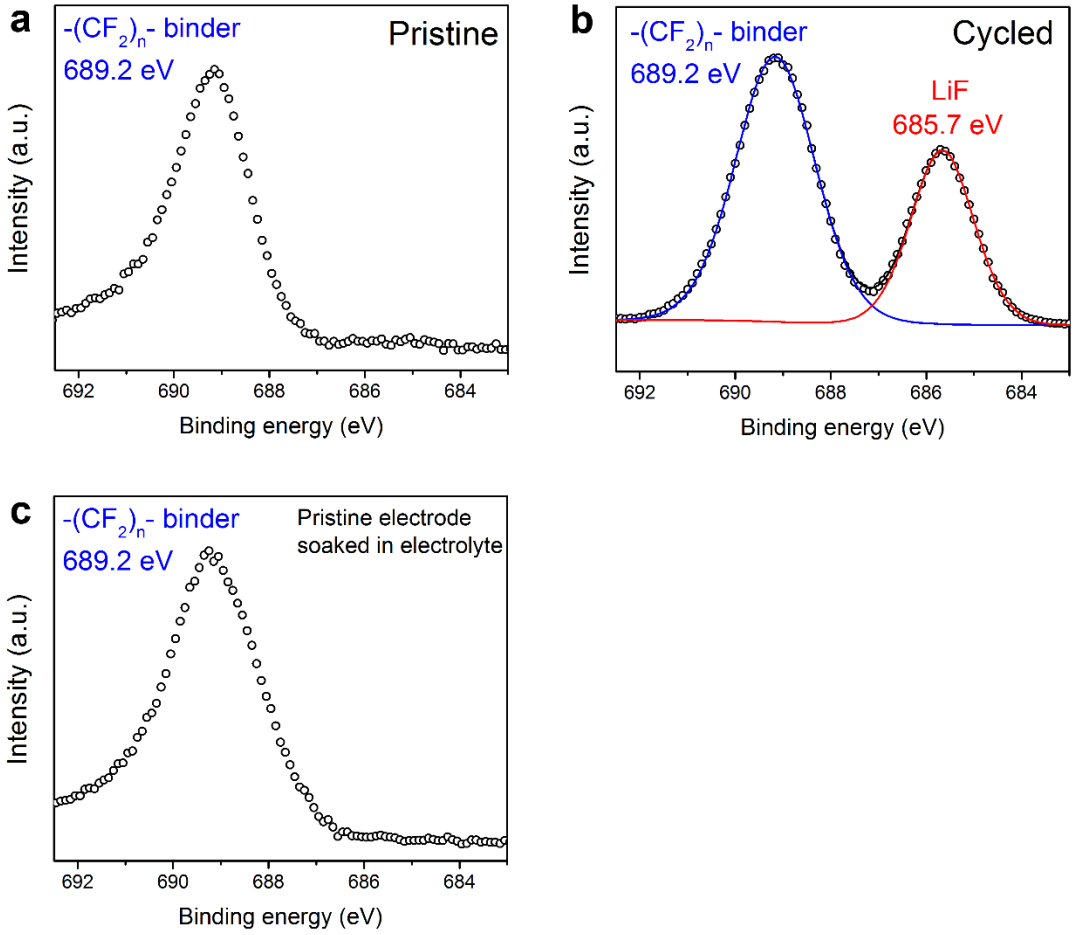

Figure S5. *Ex-situ* XPS F 1*s* spectra of S/KB anode in full cell (a) before and (b) after 20 cycles. (c) A pristine anode as control group was soaked in WiBS electrolyte without cycling. Black dotted lines are experimental data, and solid lines in other colors are fitted individual environments: -$(CF_2)_n$- 689.2 eV and LiF 685.7 eV. The pristine anode only showed a single peak at 689.5 eV, resulting from the poly(tetrafluoroethylene) (PTFE) used as binder in the composite electrode. After three full lithiation cycles, an additional peak of F 1*s* at 685.7 eV corresponding to F^- in LiF was detected, indicating that a LiF-rich interphase has been formed and covered the S-KB composite surface, which serves as an electron barrier and prevents the reduction of water while allowing Li^+ migration (13, 14). The possibility that LiF is created by X-ray irradiation as an artifact was ruled out by a control experiment, where a pristine anode soaked in WiBS electrolyte without cycling generated an XPS spectrum in absence of the 685.7 eV peak (Fig. S5c).

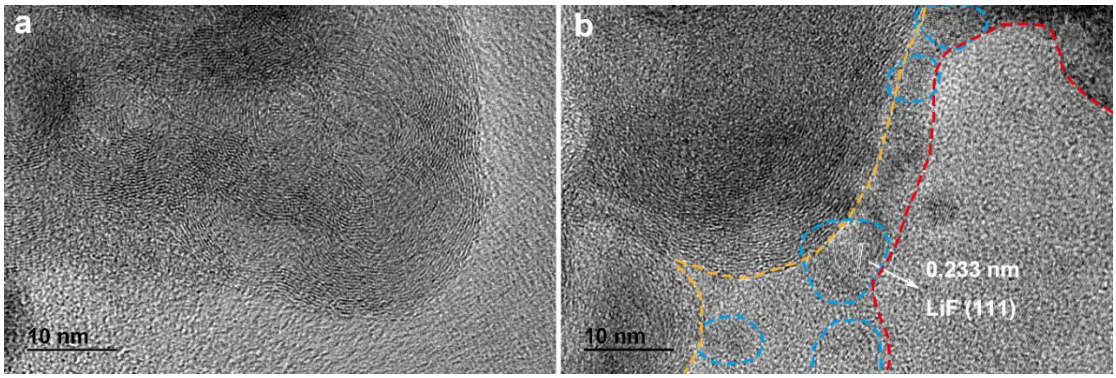

Figure S6. High-resolution TEM images of S-KB (a) before and (b) after 20 cycles at 0.2 C. Yellow and red dash lines denoted outer and inner edge of SEI layer, dotted circles marked the crystal domain of SEI in anode surface. The KB showed a typical onion-like lattice pattern with clear edges before cycling. After 20 cycles at 0.2 C, TEM clearly imaged that KB was entirely covered by a layer of numerous nano-LiF particles that would constitute a uniform SEI of 5–10 nm thick. The isolated nano-sized crystalline particles show the interplanar space of ~ 0.233 nm, which is attributed to (111) interplanar spacing of LiF.

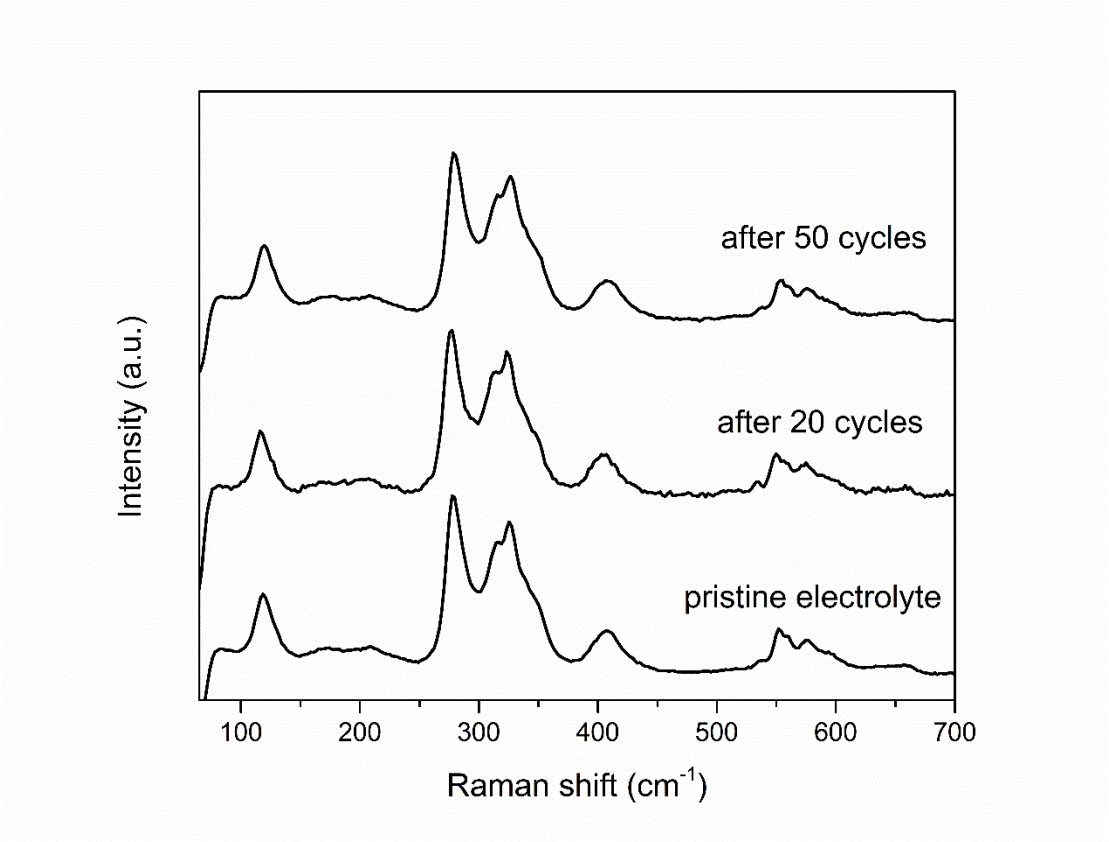

Figure S7. *In-situ* Raman spectra of 21 mol kg^{-1} LiTFSI + 7 mol kg^{-1} LiOTf aqueous solution (WiBS electrolyte) in full cell before and after 20 and 50 cycles at the rate of 0.5C.

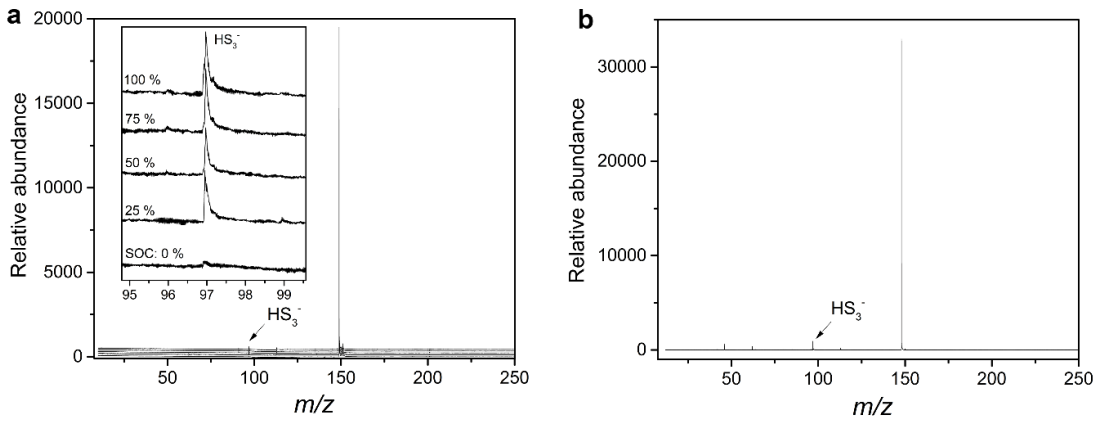

Figure S8. (a) Mass spectra of the electrolyte recovered from the cells which were charged to the different SOC at 0.1 C and then diluted by50 times. According to calculated *m/z* values of all possible sulfur species which might exist in aqueous solution (Table S1), only one peak (*m/z* = 64.95) was identified to be HS_3^- species, appearing in all the electrolyte samples from charged cells. (b) Mass spectrum of 10 μM Li_2S_4 dissolved in WiBS electrolyte diluted by 50 times as a control. The ratio of HS_3^- to the main peak in charged cell is smaller the one in the control sample, indicating that the solubility of sulfur species (only HS_3^-) in the WiBS electrolyte during cycling is < 0.5 mM (~ 71 ppm). It serves as another solid evidence that the reaction intermediate polysulfides are immiscible with the WiBS electrolyte. One additional interesting finding is that, even in WiBS electrolyte diluted by 50 times (~ 0.28 M of LiTFSI and LiOTf), the solubility of Li_2S_4 is still as low as 5 mM, as compared with the high solubility (> 4M) of Li_2S_4 in neat water.

Table S1. Calculated *m/z* values of all possible sulfur species which might exist in aqueous solution.

Species	***m/z***	**Species**	***m/z***	**Species**	***m/z***
S^{2-}	15.98604	HS^-	32.97990	LiS^-	37.98719
S_2^{2-}	31.97207	HS_2^-	64.95197	LiS_2^-	69.95923
S_3^{2-}	47.95811	HS_3^-	96.92404	LiS_3^-	101.93133
S_4^{2-}	63.94414	HS_4^-	128.89611	LiS_4^-	133.90341
S_5^{2-}	79.93018	HS_5^-	160.86818	LiS_5^-	165.87548
$S_3^{\cdot-}$,S_6^{2-}	95.91621	HS_6^-	192.84025	LiS_6^-	197.84755
S_7^{2-}	111.90225	HS_7^-	224.81232	LiS_7^-	229.81962
S_8^{2-}	127.88828	HS_8^-	256.78439	LiS_8^-	261.79169

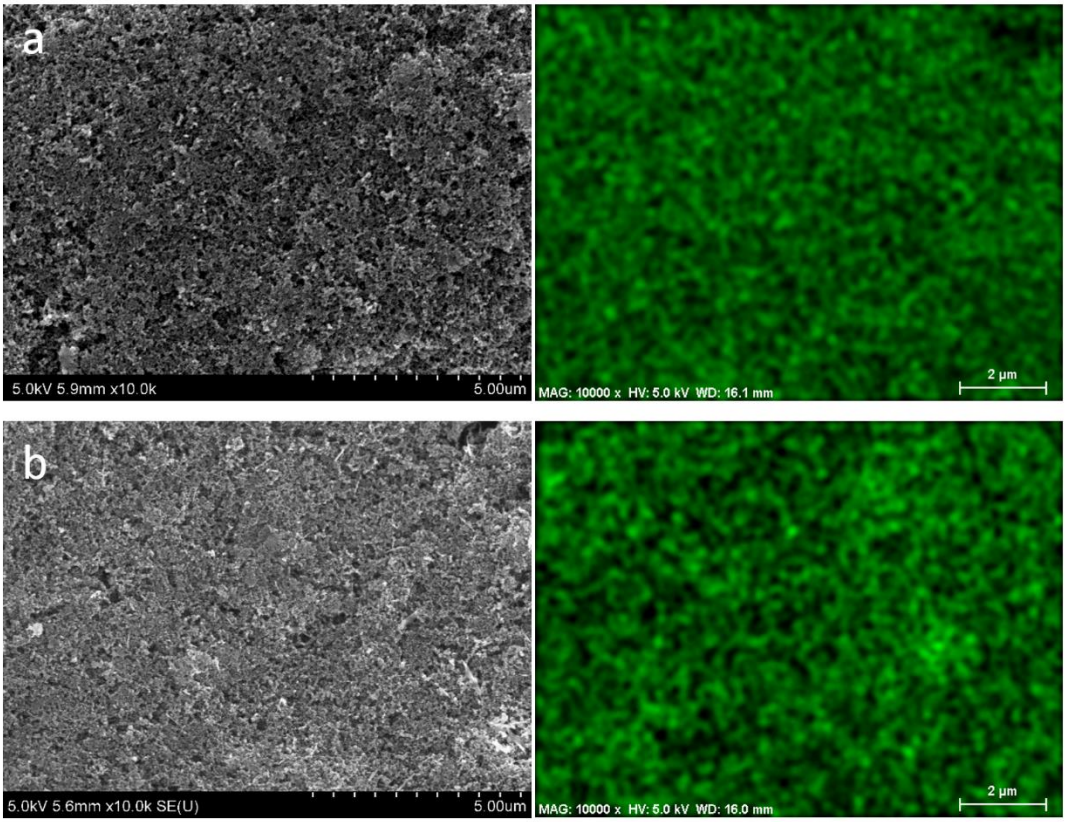

Figure S9. SEM images of S/KB anode (left) and energy-dispersive X-ray spectroscopy (EDX) analysis of sulfur (green) after (a) 1st charge and (b) 20th charge at the rate of 0.5C.

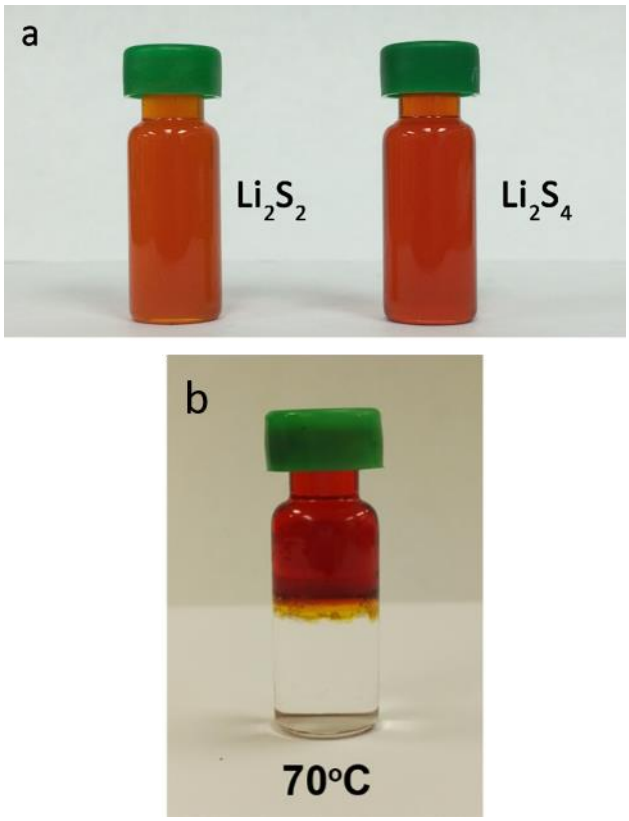

Figure S10. Photos of (a) 4m Li_2S_2 and Li_2S_4 aqueous solutions. (b) Visual observation of the insolubilities for short-chain LiPS (Li_2S_4) in WiBS electrolyte at 70 °C for 5 days, respectively.

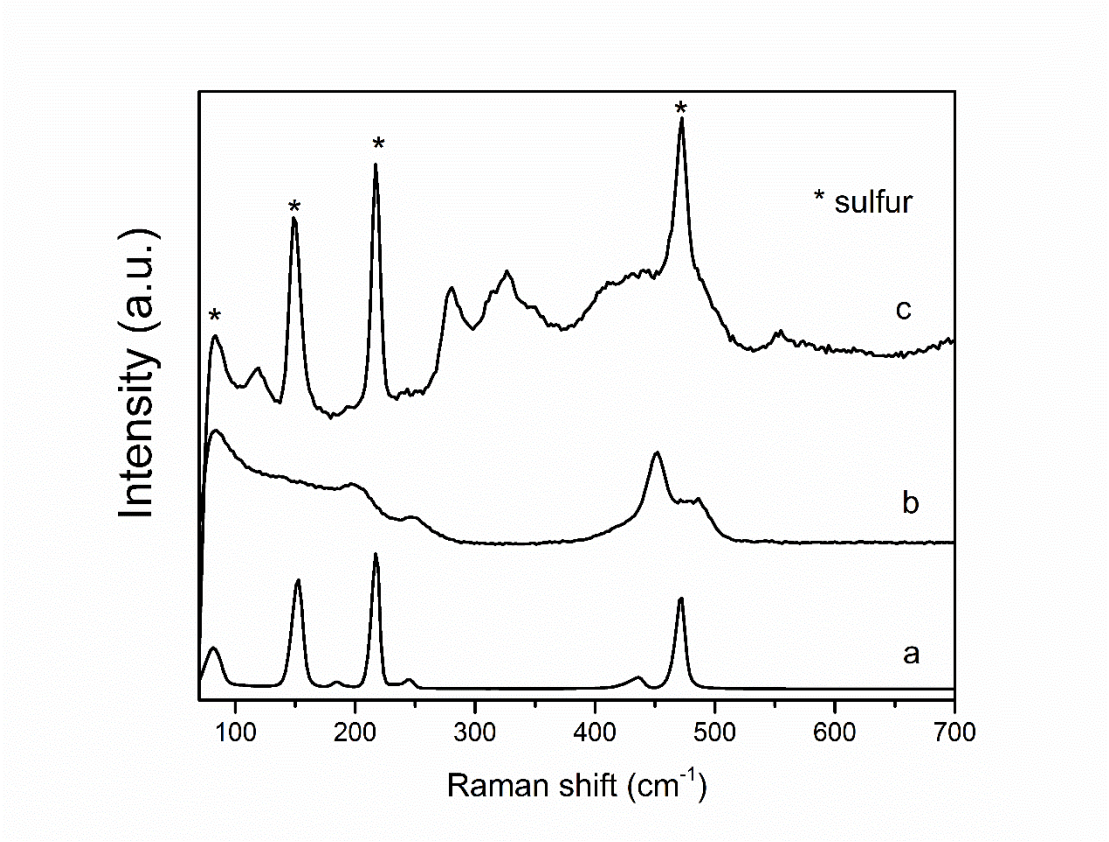

Figure S11. Raman spectra for (a) the bottom part (clear solution) and (b) the top part (jacinth color) in the mixture solution of LiPS solution and 21 mol kg^{-1} LiTFSI + 7 mol kg^{-1} LiOTf electrolyte in Fig. 2d, and (c) the solid white particles diffused into the bottom part of the mixture of LiPS solution and 21 mol kg^{-1} LiTFSI + 7 mol kg^{-1} LiOTf electrolyte. The peaks marked by stars were determined as elemental S_8.

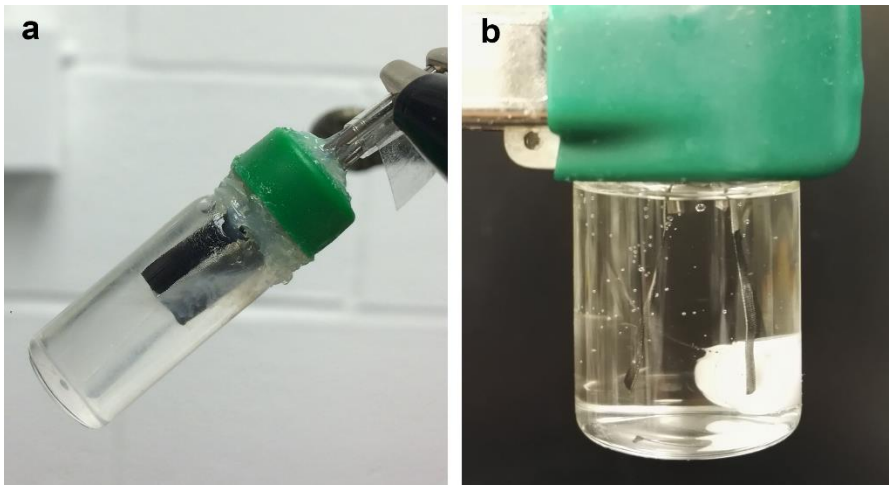

Figure S12. Photos of an S-KB and $LiMn_2O_4$ full cell assembled in a quartz bottle with (a) liquid WiBS electrolyte and (b) WiBS GPE after 200 cycles at 0.5C. A cluster of white small solid particles diffusing into the electrolyte is clearly shown in cell (a). However, no trace of solid particles showed in GPE in cell (b). A few air bubbles were trapped in GPE during assembling of cell (b).

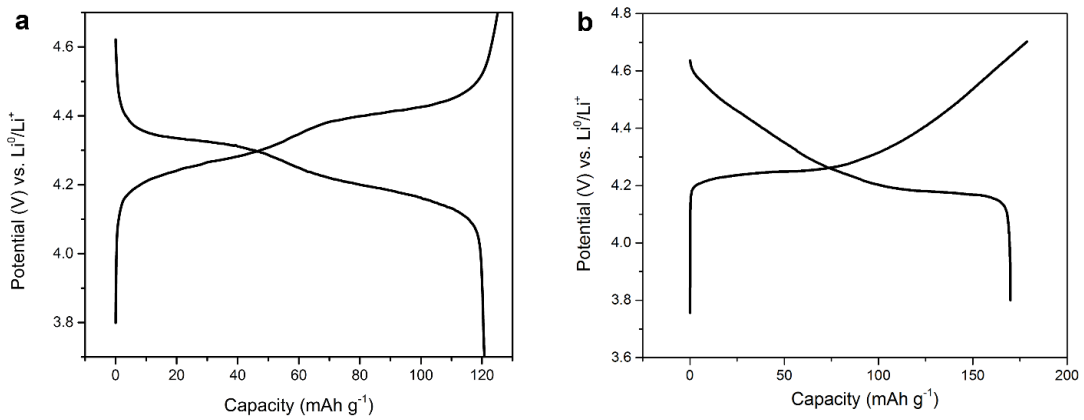

Figure S13. Typical voltage profiles of (a) $LiMn_2O_4$ and (b) HV-$LiCoO_2$ at constant current (0.2C) in 21 mol kg^{-1} LiTFSI + 7 mol kg^{-1} LiOTf solution as aqueous electrolyte. Collected in a three-electrode device with sulfur/carbon composite as working electrodes, and Ag/AgCl as reference electrode. The specific capacities are based on the mass of active materials.

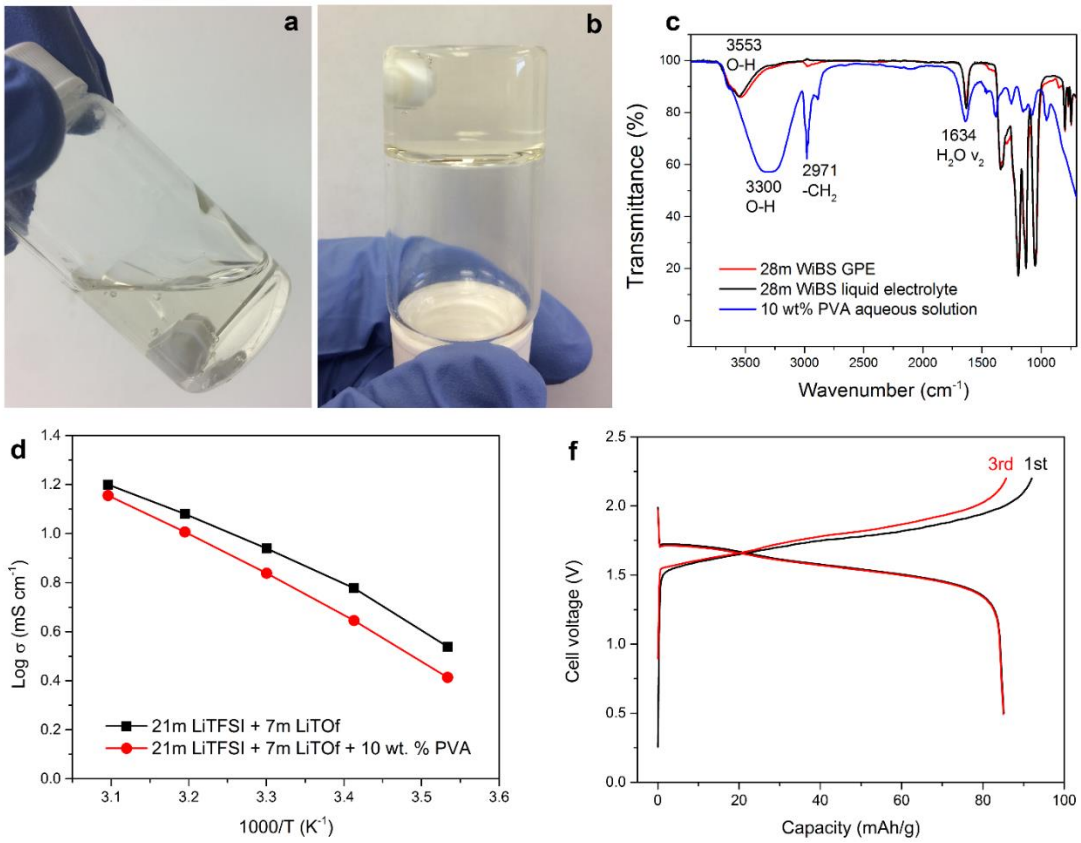

Figure S14. Photos of the transparent WiBS GPE (a) at 95°C (being taken out from oil bath) and (b) at room temperature. (c) Fourier transformed infrared spectroscopy (FTIR) of 28 mol kg^{-1} WiBS GPE, 28 mol kg^{-1} WiBS liquid electrolyte and 10 wt% PVA aqueous solution. (d) Arrhenius plots of lithium ion conductivity (σ) for WiBS liquid electrolyte and GPE in temperature range of 10°C ~ 50°C. (f) Voltage profiles of full cell with S-KB anode and $LiMn_2O_4$ cathode in WiBS GPE at current densities of 0.2C.

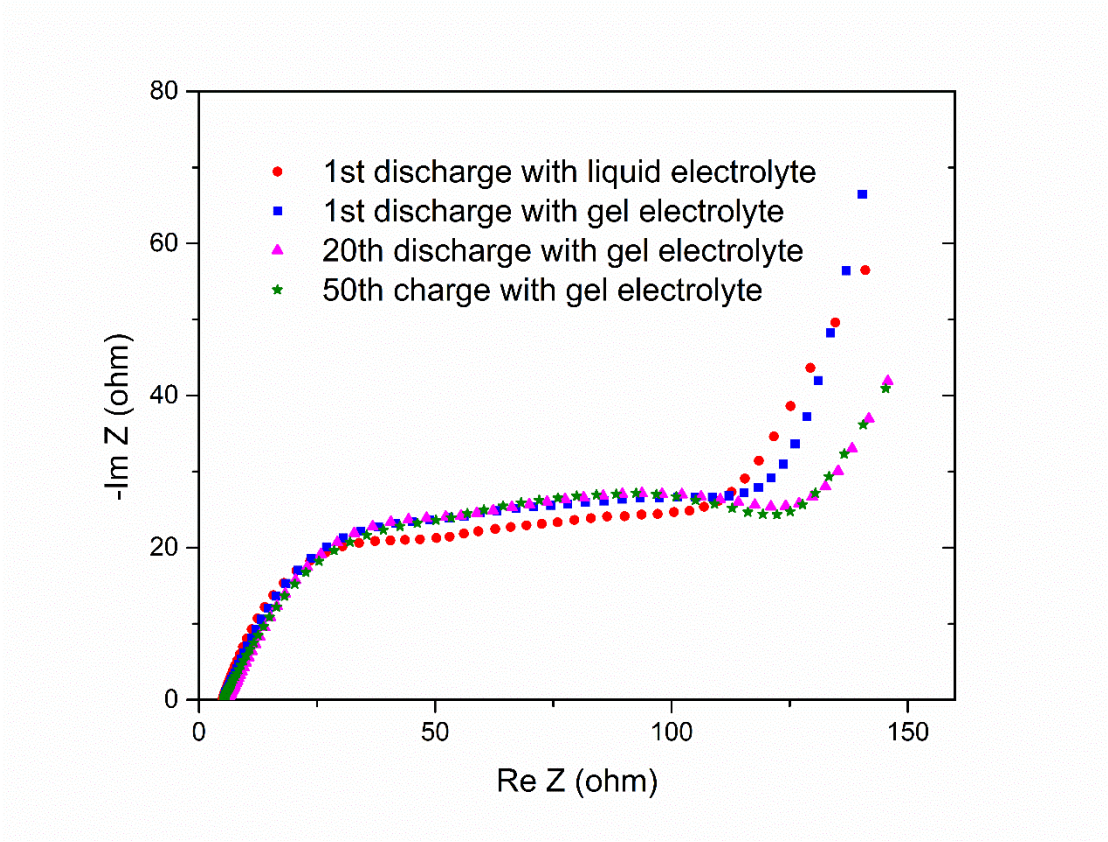

Figure S15. Electrochemical impedance spectroscopy (EIS) of S-KB/$LiMn_2O_4$ full cell with liquid and gel electrolytes at different cycles at 0.5C.

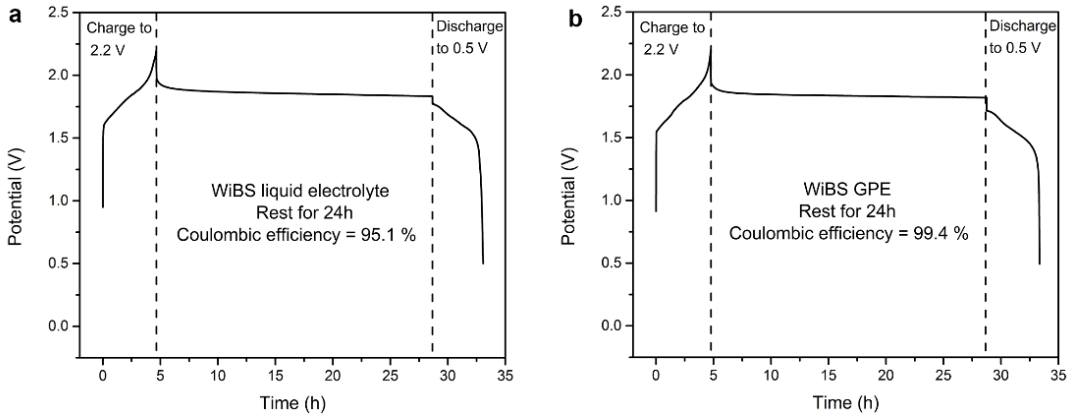

Figure S16. The OCV decays in 24-hour rest of the full cells with the (a) liquid and (b) gel electrolyte at fully charged state of 2.2 V at 0.2C, respectively. The self-discharge was evaluated by comparison with the columbic efficiency and the capacity loss after resting.

Table S2. Comparisons of aqueous Li-ion/S batteries with modern commercial Li-ion battery. The energy density calculations were based on the theoretical specific capacities of active materials.

	$LiCoO_2$/graphite	HV-$LiCoO_2$/S-KB (this work)			
Electrolyte	flammable carbonate base	aqueous			
Cell voltage	3.7 V	1.64 V			
Anode carbon ratio		70 %	50 %	30 %	0 %
Energy density (Wh/kg)	376	220	245	257	267

Calculation details:

Theoretical specific capacities:

$LiCoO_2$: 140 mAh/g

Graphite: 372 mAh/g

HV-$LiCoO_2$: 180 mAh/g

Sulfur: 1675 mAh/g

The energy density of electrochemical couples:

$LiCoO_2$/Graphite: 3.7 V × 1/ (1/140 mAh/g +1/372 mAh/g) = 376 Wh/Kg

HV-$LiCoO_2$/S-KB (70 % carbon): 1.64 V × 1/ (1/180 mAh/g +1/503 mAh/g) = 217 Wh/Kg

HV-$LiCoO_2$/S-KB (0 % carbon): 1.64 V × 1/ (1/180 mAh/g +1/1675 mAh/g) = 267 Wh/Kg

Quantum Chemistry Study of Lithium Polysulfide Protonation and Lithium Dissociation

Strategies for selecting electrolytes to limit polysulfide solubility have been recently reviewed (1), outlining the design rules for maximizing solubility of the supporting salt (e.g. LiTFSI, $LiCF_3SO_3$) and minimizing lithium polysulfide. The suggested strategies fall largely within two categories: a) limited solvent and b) selective solvent design to achieve sparingly solvating electrolytes. In the case of aqueous electrolytes the solvent is specified, it is water. Thus, the solvent limitation strategy is pursued (2, 3) together with the anode coating by SEI. Weakly associating [with Li^+] anions such as bis(trifluoromethane)sulfonamide ($TFSI^-$) or bis(fluorosulfonyl)imide (FSI^-) preferentially dissociate over lithium polysulfide s and were shown to result in the reduced polysulfide solubility in concentrated electrolytes (4). The gas-phase cation-anion binding energy is an often used approximate marker for the salt dissociation (5, 6). We first discuss the relative binding energies of the Li_2S_2, Li_2S_4, LiTFSI and $LiCF_3SO_3$ salts in gas-phase and follow up with the more rigorous study of the free energy for the Li^+ cation dissociation using a cluster – continuum approach that takes into account solvent effects. The later are introduced by explicitly including the solvent molecules immediately interacting with the anion or lithium as well as the polarized continuum model (PCM) to account for water that was not included explicitly. The PCM model using water parameters was used in all calculations as implemented in Gaussian g09 (revision c) package unless stated otherwise (7).

In gas-phase the Li^+ binding energy to the $TFSI^-$ anion is around -135 kcal/mol (-5.88 eV) (8), which is much lower than the first Li^+ dissociation energy for Li_2S_4 of -148.8 kcal/mol (-6.45 eV) and second lithium dissociation energy of -253.0 kcal/mol (-10.97 eV) obtained from G4MP2 quantum chemistry (QC) calculations relative to the singlet states of LiS_2^- and $S_2^{(2-)}$ as shown in Fig. S17. The first Li^+ dissociation energy from Li_2S_2 is even higher that the Li_2S_4 dissociation energy. It is -161.9 kcal/mol from G4MP2 calculations in gas-phase, suggesting the preferential dissociation of the LiTFSI salt compared to Li_2S_4 polysufide and especially Li_2S_2. The lithium binding energy in $LiCF_3SO_3$ is -138.6 kcal/mol (-6.01 eV) at G4MP2 level (9), which is higher than the binding energy in LiTFSI but still much lower than the binding energy in Li_2S_2 or Li_2S_4.

$\Delta E(Li_2S \rightarrow LiS^- + Li^+)$
G4MP2 -166.1
MP2/Tz -167.9
FF -167.1

$\Delta E(Li_2S_2 \rightarrow LiS_2^- + Li^+)$
G4MP2 -161.9
MP2/Tz -163.2
FF -162.3

$\Delta E(Li_2S_4 \rightarrow LiS_4^- + Li^+)$
G4MP2 -148.8
MP2/Tz -150.1
FF -151.1

$\Delta E(LiS_4^- \rightarrow S_4^{2-} + Li^+)$
G4MP2 -253
FF -253.4

Figure S17. The Li^+ binding energies for the Li_2S_x clusters from quantum chemistry calculations using G4MP2, Møller–Plesset perturbation theory (MP2)/aug-cc-pvTz (denoted as MP2/Tz) methods and molecular mechanics using developed force field (denoted FF) in kcal/mol.

Next, the Li^+ cation dissociation from sulfide s was examined for the representative Li_2S_x –based (x=1, 2, 4) sulfide complexes using a cluster – continuum approach. The PBE/6-31+G(d,p) density functional theory method and G4MP2 were used as implemented in g09 Gaussian package. PBE functional was chosen as it was found to adequately describe Li-solvent binding energy (10) and is significantly less computationally expensive than the more accurate G4MP2 composite methodology that was also utilized.

We begin by examining Li_2S_2-$(H_2O)_6$ clusters immersed in implicit solvent modelled via PCM(water) and focus on the energetics of the Li^+ cation dissociation and proton transfer to anion as a result of water coordination. The relative binding energies from G4MP2 and PBE/6-31+G(d,p) calculations are shown in Fig. S18. The following scenarios were investigated: 1) an anion associated with the Li^+ and H^+ cations (LiS_2H: complex-a); 2) an anion associated with Li^+ but not H^+ (LiS_2: complexes b-c); 3) an anion that is solvent separated from the Li^+ cation and H^+ ($S_2^{(2-)}$: complexes d-f) and 4) the anion associated only with protons but solvent separated from Li^+ (S_2H: complexes g-h). QC calculations show that the LiS_2^- complexes (b-c) tend to be slightly less stable than the S_2^- anions with the Li^+ cations separated by water molecules (complexes d-f). The later complexes are among the most stable solvates. These results indicate that the Li_2S_2 salt in water is likely to be have a significant fraction of anions with both Li^+ dissociated from it when a sufficient amount of free water is available. Excess water is also going to result in water decomposition and LiS_2H and HS_2^- formation as evident from the high relative stability of complexes (a) and (g). The S_2H^- complexes (g-h) are slightly less stable than the complexes where S_2^{2-} is formed. Based upon

QC calculations, stability of the Li_2S_2-based solvates could be approximated as follows: $S_2^{2-} \approx S_2H^- > LiS_2H > LiS_2$. We conclude that when free water is available, both Li^+ cations are likely to dissociate from Li_2S_2, while the S_2H^- and LiS_2H solvates are also expected to be present.

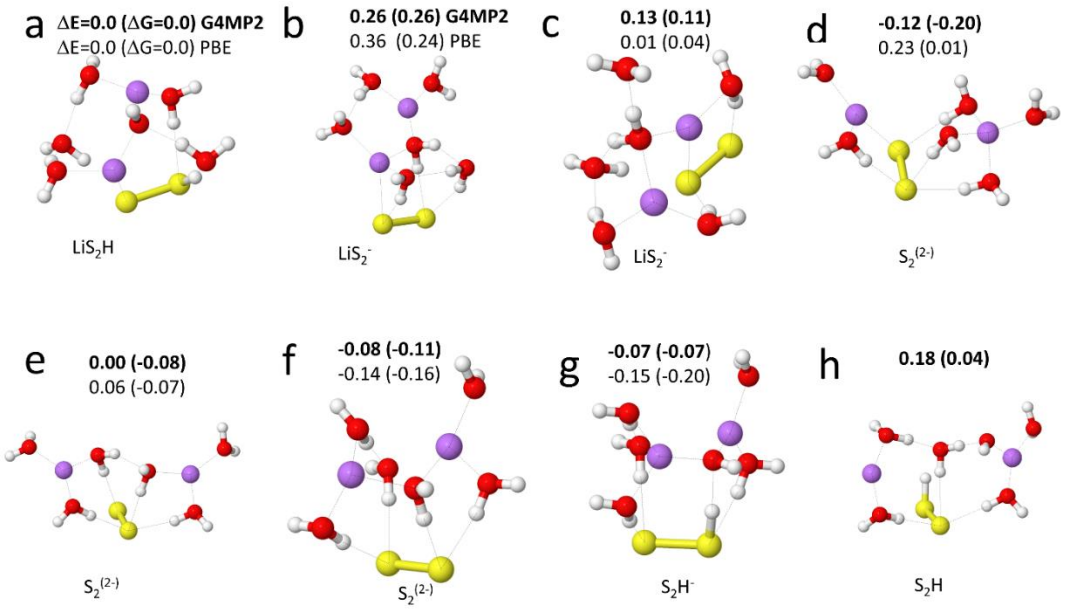

Figure S18. Relative energies (ΔE) and free energies (ΔG, in parentheses) for the Li_2S_2-$(H_2O)_6$ solvates from G4MP2 (in bold) and PBE/6-31+G(d,p) QC calculations in eV. PCM(water) polarized continuum model was utilized in all calculations.

The Li^+ dissociation and water decomposition in the longer Li_2S_4 polysulfide was examined using the Li_2S_4-$(H_2O)_8$ complexes as a model system as shown in Fig. S19. Again, PCM model was utilized to implicitly include solvent effects beyond the first eight water molecules that were explicitly included in QC calculations. We find that the contact ion pair (CIP, complexes a-c) LiS_4^- has a similar or even slightly higher energy than the fully dissociated complexes (d-f). All examined HS_4^- solvates (complexes g-j) have higher energy and lower stability than the SSIP $S_4^{(2-)}$ or LiS_4^- solvates indicating that water deprotonation near longer polysulfide s such as Li_2S_4 is unlikely. Water decomposition is, however, energetically favorable on the surface of $(Li_2S)_3$ clusters as shown in Fig. S20. Single protonation of the (Li_2S) clusters stabilizes them by as much as 0.39 eV when free water is available. Due to improved stability such clusters will form earlier during cell charging resulting in a flatter charging profile compared to standard aprotic electrolytes as shown in Fig. 2(C-D) in the main part of the manuscript.

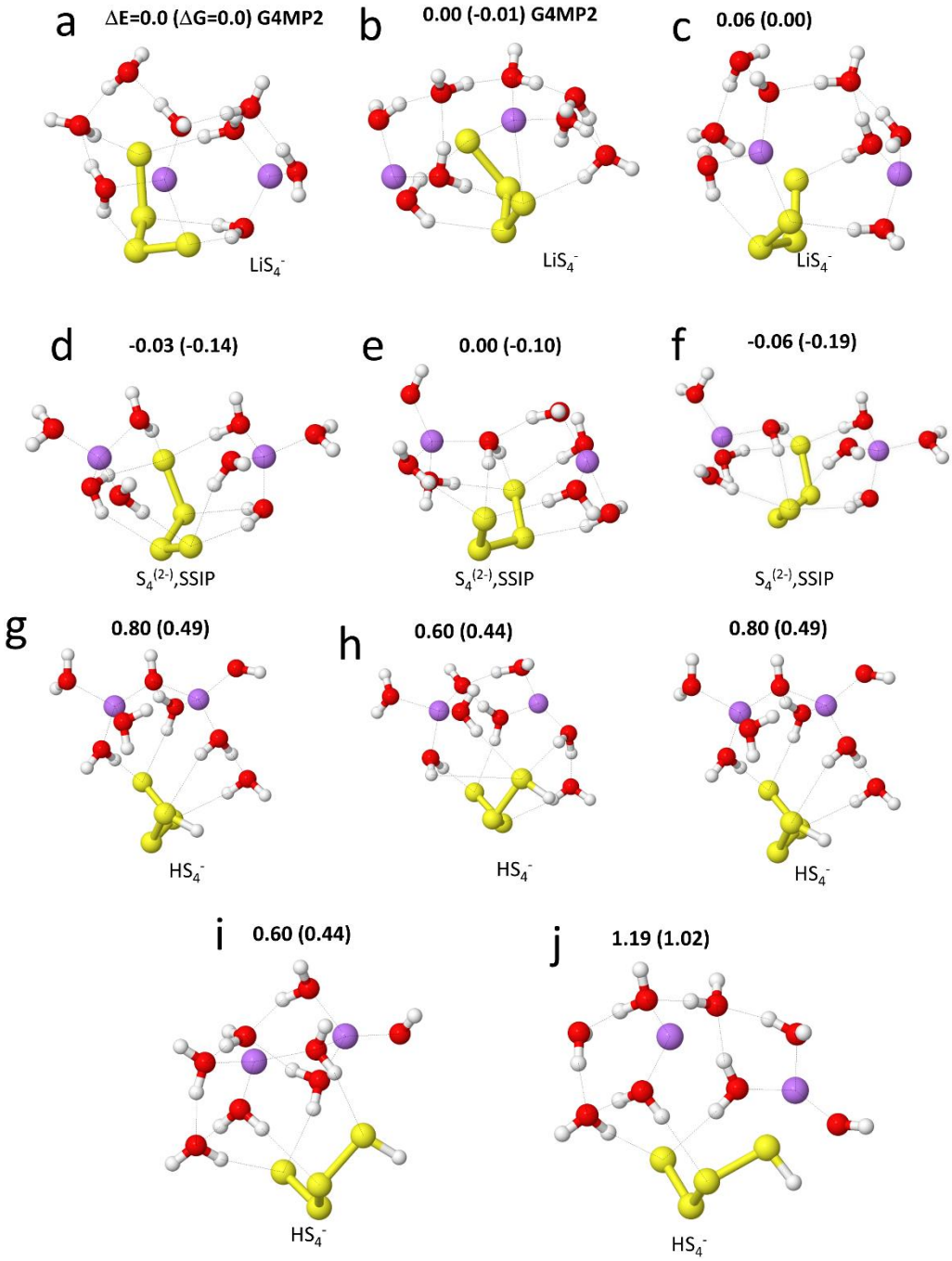

Figure S19. Relative energies (ΔE) and free energies (ΔG, in parentheses) for the Li_2S_4-$(H_2O)_8$ solvates from G4MP2 QC calculations in eV. PCM (water) polarized continuum model was utilized in all calculations.

In summary, we conclude that strong lithium dissociating propensity of water facilitates the Li_2S_2 and Li_2S_4 dissolution, suggesting that limiting the amount of free water is necessary to suppress Li_2S_2 and Li_2S_4 association, encourage aggregation and potentially to suppress their

solubility in aqueous electrolytes and hence reduce water decomposition. Short chain polysulfide s (Li_2S, Li_2S_2) are stabilized by water decomposition followed by H-S bond formation, while OH- and HS_4^- formation is energetically unfavorable for the longer chain polysulfide such as Li_2S_4.

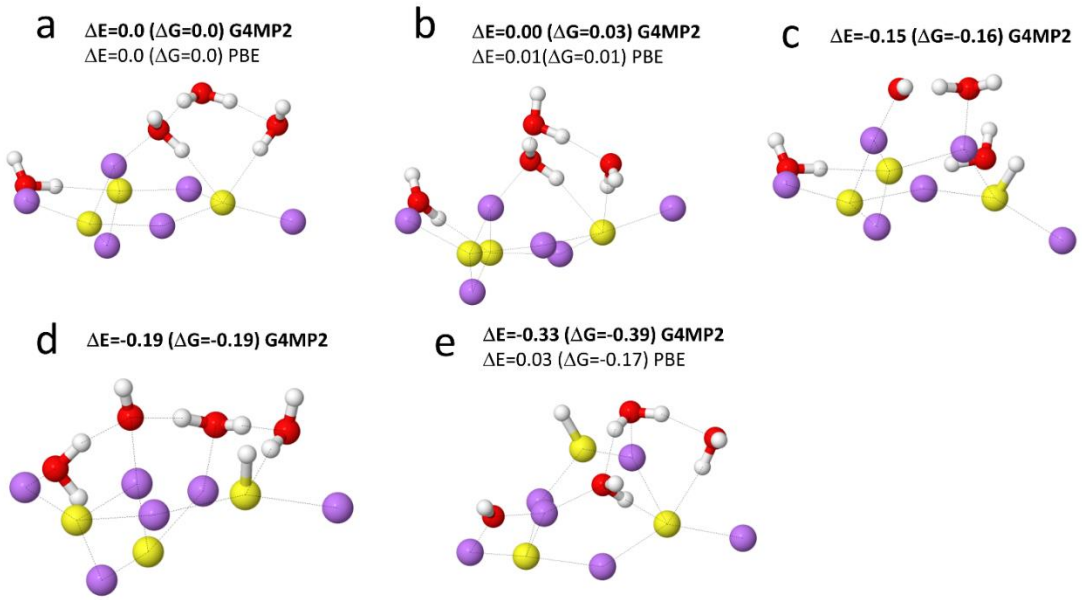

Figure S20. Relative energies (ΔE) and free energies (ΔG, in parentheses) for the $3Li_2S$-$(H_2O)_4$ solvates from G4MP2 (in bold) and PBE/6-31+G(d,p) QC calculations. PCM(water) polarized continuum model was utilized in all calculations.

In order to further examine the relative stability of the Li_2S_2 vs. Li_2S_4 solvates, free energy of the following reaction was calculated using the lowest energy solvates from Figures S18-S19 using eq. S1 that is equivalent to eq. S2:

$$Li_2S_4(H_2O)_8 + 2Li^+(H_2O)_4 \rightarrow 2(Li_2S_2(H_2O)_6) + (H_2O)_4 \quad \text{(S1)}$$

$$Li_2S_{4SOLV} + 2Li^+_{SOLV} \rightarrow 2(Li_2S_2)_{SOLV}, \quad \text{(S2)}$$

where the subscript SOLV denotes the solvated and dissociated species in electrolyte. This reaction was found exergonic with reaction free energy of -0.29 eV. Thus, the dissociated Li_2S_4 will convert to Li_2S_2 $+2Li^+$ (solvated) in aqueous electrolytes and the polysulfide equilibrium is shifted to shorter chain polysulfide molecules. Interestingly, previous DFT studies showed formation of Li_4S_8-like agglomerate in the LiTDI-salt based electrolyte that was more stable and compact than the

polysulfides formed in the LiTFSI-salt electrolyte indicating that a choice of anion could also influence polysulfide aggregation and disproportionation reactions (11).

Molecular Dynamics Simulations of Polysulfide s in Water and Bisalt Electrolyte

Force field for the Li_2S_2 and Li_2S_4 polysulfide salts was developed in this work following previously established methodology (12). It accurately described the Li^+ binging energy for the Li_2S_x (x=1, 2, 4) as shown in Fig. S17 and water binding energy to S_4^-. The $H_2O/S_4^{(2-)}$ binding energy was -19.5 kcal/mol from molecular mechanism using developed force field that is only slightly lower than the binding energy of -20.5 kcal/mol obtained from G4MP2 QC calculations. The previously developed and valided LiTFSI/water and $LiCF_3SO_3$/water force field parameters were used (13, 14). The Li^+ cation charge being set to 1e while the $TFSI^-$ and $CF_3SO_3^-$ anion charges were set to -1e. The Ewald summation method was used for the electrostatic interactions between permanent charges with permanent charges and permanent charges with induced dipole moments with $k = 7^3$ vectors. Multiple timestep integration was employed with an inner timestep of 0.5 fs (bonded interactions), a central time step of 1.5 fs for all nonbonded interactions within a truncation distance of 7.0-8.0 Å and an outer timestep of 3.0 fs for all nonbonded interactions between 7.0 Å and the nonbonded truncation distance of the smaller of 16 Å. The reciprocal part of Ewald was updated only at the largest of the multiple time steps. A Nose-Hoover thermostat and a barostat were used to control the temperature and pressure with the associated frequencies of 10^{-2} and 0.1 x 10^{-4} fs.

The in-house developed MD simulation package that includes many-body polarization, was used for all the MD simulations. Four electrolytes were simulated: (a) 4m Li_2S_2 in water; (b) 4m Li_2S_4 in water; (c) 4m Li_2S_2 in 21 mol kg^{-1} LiTFSI + 7 mol kg^{-1} $LiOCF_3SO_3$ denoted as 4m Li_2S_2 in water in bisalt salt electrolyte (WiBS); and (d) 4m Li_2S_4 in 21 mol kg^{-1} LiTFSI + 7 mol kg^{-1} $LiOCF_3SO_3$ denoted as 4m Li_2S_4 in WiBS. The MD simulation box comprised of 112 Li_2S_x (x=2,4) and 1536 waters for 4m salt in water electrolytes and 56 Li_2S_x (x=2,4), 96 $LiCF_3SO_3$, 288 LiTFSI and 768 waters for the polysulfide s in WiBS electrolytes. The initial configurations for simulations were created in the gas-phase with box sizes around 100 Å for the WiBS-based electrolyte and 75 Å for the sulfide s in water electrolytes. The simulation box dimensions were gradually decreased to 55 Å during 1 ns run at 500 K. Than the temperature was dropped to 450 K and NPT equilibration

runs were performed for 1.5 ns for 4 m Li_2S_4 in water electrolyte and 5 ns for Li_2S_4 in WiBS electrolyte using the force field with an additional repulsion between sulfides to facilitate their even distribution through the simulation box. The initial configurations of the Li_2S_2 in water and Li_2S_2 in WiBS electrolytes were generated from the final configurations of the corresponding systems with Li_2S_4 by removing two sulfur atoms from the S_4-chain. After that MD simulations were performed in order to examine the lithium polysulfide dissociation, aggregation and nano-separation. MD simulations of Li_2S_4 in WiBS were performed for 45 ns at 333 K. Since the experimental results also showed a sharp phase separation around 333 K (Fig. S8d), the higher temperature can accelerate MD simulations. Li_2S_4 in water was initially simulated for 4.0 ns at 363 K followed by 4.4 ns simulations at 333 K. MD simulations of Li_2S_2 in WiBS were performed for 8.0 ns at 393 K followed by 3.0 ns run at 333 K, while Li_2S_2 in water was simulated for 2 ns at 333 K. The initial and final configurations for the Li_2S_2 and Li_2S_4 in WiBS electrolytes and for Li_2S_2 and Li_2S_4 in water are shown in Fig. S21 and S22, respectively, highlighting the polysulfide anions and water.

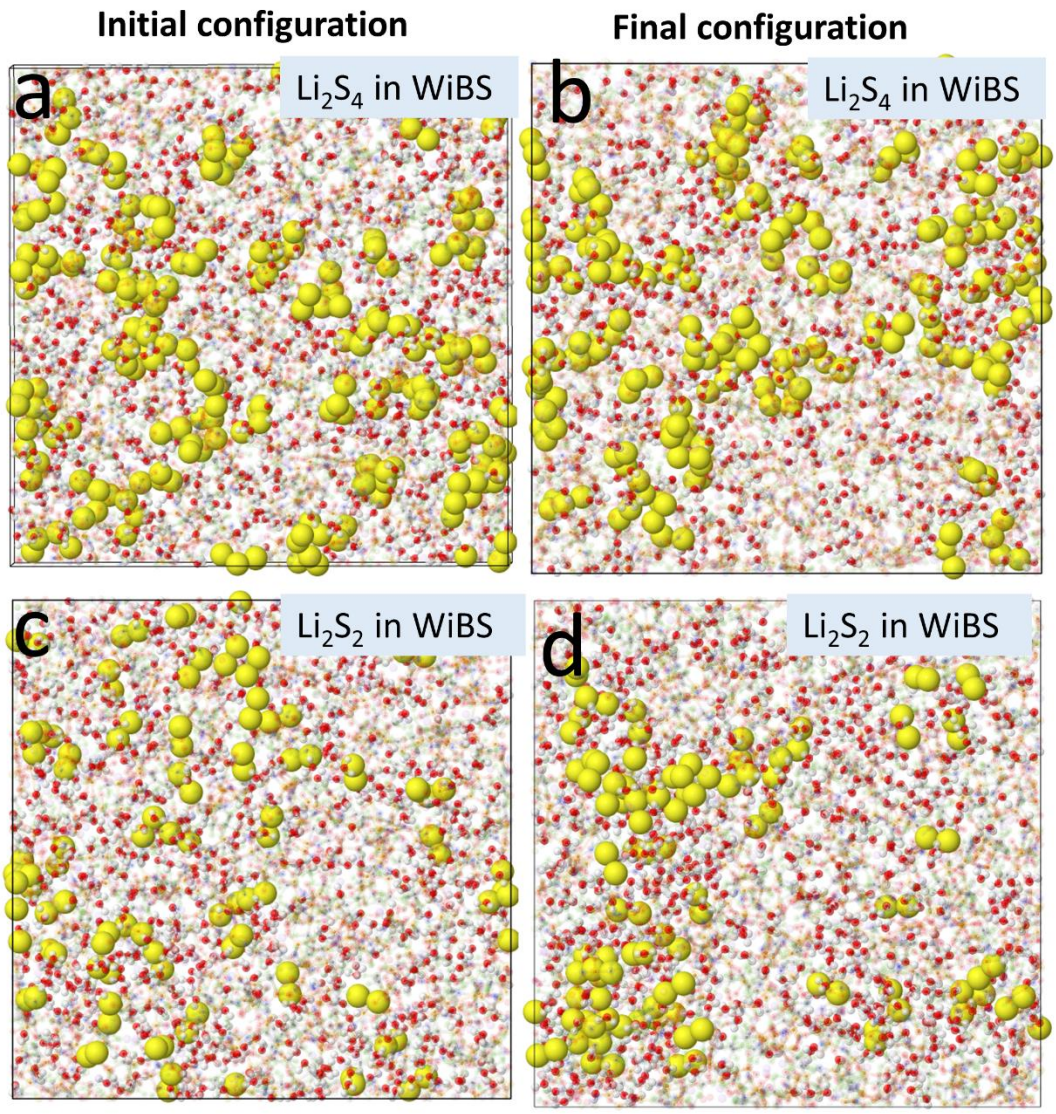

Figure S21. Projections of MD simulation boxes highlighting Li_2S_4 and Li_2S_2 polysulfide anions (color yellow) and water (color O:red, H:white) separating in WiBS electrolyte. Initial configurations (a,c) and final configurations (b,d) of MD simulations are shown.

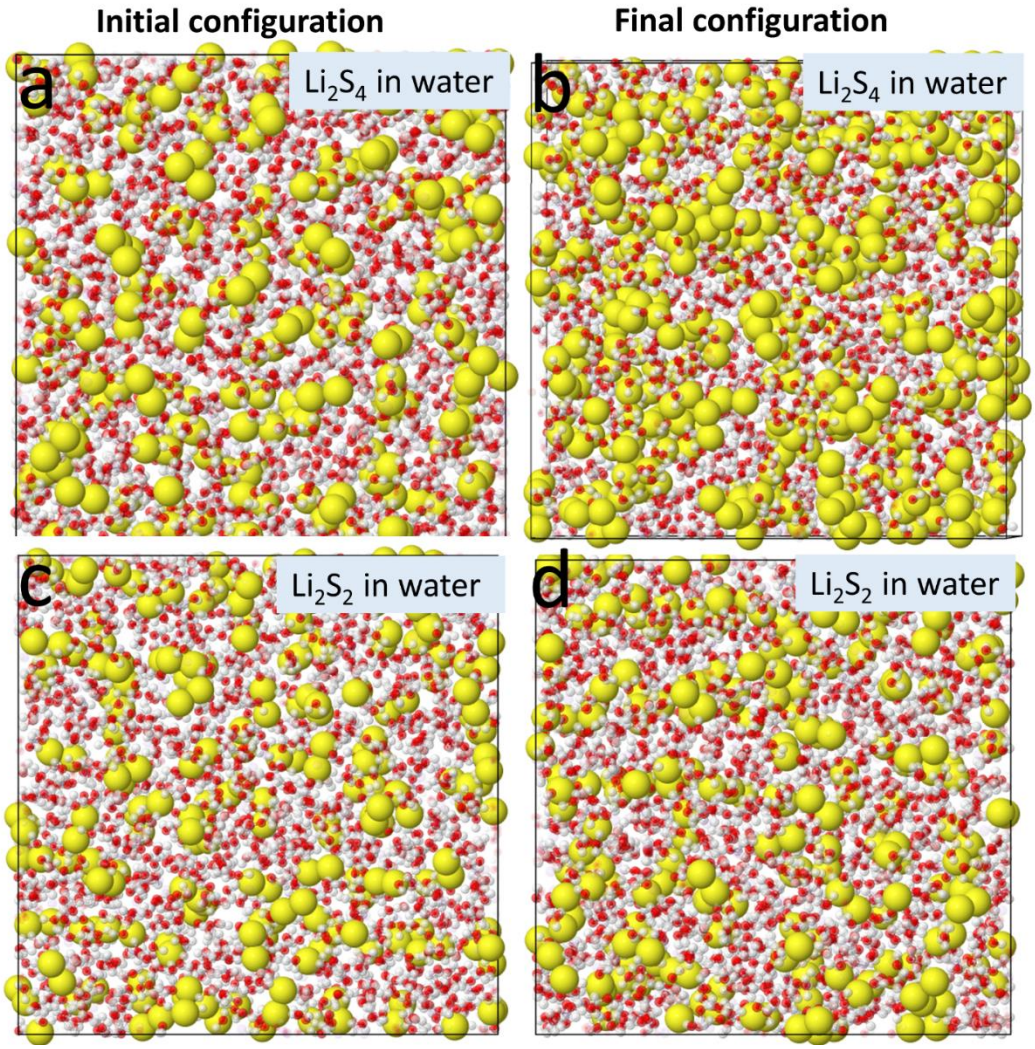

Figure S22. Projections of MD simulation boxes highlighting Li_2S_4 and Li_2S_2 polysulfide anions (color yellow) and water (color O:red, H:white) for Li_2S_4 in water (a-b) and Li_2S_2 in water (c-d). Initial configurations (a,c) and final configurations (b,d) of MD simulations are shown.

The Li_2S_4 polysufides were found to increasingly aggregate and separate in the WiBS electrolytes during MD simulations runs as shown in Fig. S21b. There is a domain without $S_4^{(2-)}$ in the MD simulations box that is formed during simulations. The shorter polysulfide anions $S_2^{(2-)}$ were found to exhibit even stronger aggregation and separation in the Li_2S_2 in WiBS electrolyte in the course of MD simulations than the observed $S_4^{(2-)}$ anion separation in the Li_2S_4 in WiBS electrolyte highlighting a stronger propensity of the shorter lithium polysulfide s to aggregate and separate into domains. Fig. S21 also shows that there is an enrichment of water near the polysulfide domain

compared to the rest of electrolyte indicating that water limitation is likely to limit the size of the solvated polysulfide domain. MD simulations of the Li_2S_2 and Li_2S_4 4m polysulfide solutions in water shows in Fig. S22 that both Li_2S_2 and Li_2S_4 are well dissolved and mixed. Most of the Li^+ cations were found to be solvent separated from polysulfide $S_4^{(2-)}$ and $S_2^{(2-)}$ anions in the Li_2S_2 in water and Li_2S_4 in water electrolytes in accord with QC results shown in Figures S18 and S19. We conclude that the results of MD simulations are in excellent agreement with the experimental observations showing phase separation of the lithium polysulfide s in WiBS electrolytes (see Fig. 2 of the main manuscript) and high polysulfide solubility in water.

Supplementary References

1. Cheng L, et al. (2016) Sparingly Solvating Electrolytes for High Energy Density Lithium–Sulfur Batteries. *ACS Energy Letters* 1(3):503-509.
2. Suo L, Hu Y-S, Li H, Armand M, Chen L (2013) A new class of Solvent-in-Salt electrolyte for high-energy rechargeable metallic lithium batteries. *Nat Commun* 4: 1481.
3. Lee JT, et al. (2013) Sulfur-Infiltrated Micro- and Mesoporous Silicon Carbide-Derived Carbon Cathode for High-Performance Lithium Sulfur Batteries. *Adv Mater* 25(33):4573-4579.
4. Ueno K, et al. (2013) Anionic Effects on Solvate Ionic Liquid Electrolytes in Rechargeable Lithium-Sulfur Batteries. *J Phys Chem C* 117(40):20509-20516.
5. Jonsson E, Armand M, Johansson P (2012) Novel pseudo-delocalized anions for lithium battery electrolytes. *Phys Chem Chem Phys* 14(17):6021-6025.
6. Scheers J, Jonsson E, Jacobsson P, Johansson P (2012) Novel Lithium Imides; Effects of -F, -CF_3, and -C equivalent to N Substituents on Lithium Battery Salt Stability and Dissociation (vol 80, pg 18, 2012). *Electrochemistry* 80(3):142-142.
7. Frisch MJT G W, et al. G09, Revision C. Wallingford CT, 2013: Gaussian, Inc.; 2013.
8. Bauschlicher CW, Haskins JB, Bucholz EW, Lawson JW, Borodin O (2014) Structure and Energetics of Li^+-$(BF_4^-)_n$, Li^+-$(FSI^-)_n$, and Li^+-$(TFSI^-)_n$: Ab Initio and Polarizable Force Field Approaches. *J Phys Chem B* 118(36):10785-10794.
9. Borodin O, et al. (2015) Electrolyte Solvation and Ionic Association: VI. Acetonitrile-Lithium Salt Mixtures: Highly Associated Salts Revisited. *J Electrochem Soc* 162(4):A501-A510.

10. Delp SA, et al. (2016) Importance of Reduction and Oxidation Stability of High Voltage Electrolytes and Additives. *Electrochimica Acta* 209:498-510.

11. Chen J, et al. (2016) Restricting the Solubility of Polysulfide s in Li-S Batteries Via Electrolyte Salt Selection. *Adv Ener Mater* 6(11):1600160.

12. Borodin O (2009) Polarizable Force Field Development and Molecular Dynamics Simulations of Ionic Liquids. *J Phys Chem B* 113(33):11463-11478.

13. Suo L, et al. (2015) "Water-in-salt" electrolyte enables high-voltage aqueous lithium-ion chemistries. *Science* 350(6263):938-943.

14. Suo L, et al. (2016) Advanced High-Voltage Aqueous Lithium-Ion Battery Enabled by "Water-in-Bisalt" Electrolyte. *Angew Chem Int Ed* 55(25):7136-7141.